Ni–Cu Bimetallic Oxides with Tailored Morphology for High-Performance Alkaline Water Oxidation

Anila Tabassum,[a] Sadia Ata,*[a] Yulong Ding,[b] Ijaz Ul Mohsin,[c] Sajjad Ahmed Khan Leghari,[d] Abdullah A. Al-Kahtani,[e] Ayman Nafady,[e] and Manzar Sohail*[f]

Water oxidation, a crucial step in electrochemical water splitting, is often hindered by its complex kinetics. In our pursuit of designing efficient electrocatalysts, we have found that morphological modifications during synthesis are powerful tools. By manipulating various parameters, such as reaction time and temperature, we have tuned the morphology of the catalysts, leading to a significant enhancement in the oxygen evolution reaction (OER) rate. Our thorough research involves using a simple hydrothermal method for synthesizing bimetallic Ni–Cu oxides, resulting in the emergence of different morphologies by varying reaction times from 4 to 24 h. The OER performance in an alkaline medium, using a 1 M KOH solution, has been meticulously investigated, and our results have unveiled the highest activity for Ni–Cu fabricated with a growth time of 24 h. Ni–Cu oxide 24 exhibits a remarkably low onset potential for OER at 222 mV with a Tafel slope of 373 mV/dec. The catalyst boasts the lowest R_{ct} value of 2.788 ohm, ensuring faster charge transfer rates and stability up to 1000 cyclic voltammetry (CV) cycles, thereby supporting its electrochemical applications for water splitting.

1. Introduction

Hydrogen, carrying a high calorific value of (142 MJ/kg), is considered a clean fuel for future alternatives to traditional energy resources because of its pollutant-free nature.[1] Various pathways are available for hydrogen production, such as methane reforming, gasification of coal, and water electrolysis/splitting. However, fossil-fuels-based hydrogen production drastically harms the environment through carbon dioxide exhalation. So, among these methods, water electrolysis provides hope as a sustainable pathway to produce hydrogen because water is abundant and a renewable resource.[2] The electrochemical water electrolysis/splitting mainly consists of two reactions: the hydrogen evolution reaction (HER), involving the transfer of two electrons at the cathode, and the oxygen evolution reaction (OER), which involves the transfer of four electrons at the anode. The full reaction ideally requires 1.23 V potential, but the operating cell voltage actually reaches 1.8 V. On that account, an exceptionally efficient electrocatalyst is needed to narrow down the overpotential value. Presently, Ru/Ir and Pt oxides are accepted as benchmarking catalysts for OER and HER, respectively. Nonetheless, their commercial-level usage is hindered as they are costly and scarce.[1a,3] Alternatively, nonnoble metals such as transition metals are a substitute choice.[4]

The transition metal oxides, as being inexpensive, having variable oxidation states along with coordination chemistry within the structure and being thermodynamically stable, result in commercial uses for water electrolysis.[5] However, binary transition metal oxides have recently emerged because of cationic substitutions and are attractive for water electrolysis.[6] The studies revealed that binary metal oxides, by exerting a synergistic effect, provide more active sites, bring distinctive morphological changes, and create unique interfaces for adsorption/desorption of reaction intermediates to facilitate charge transfer and insert more stability, thus helping in improving the catalytic reaction with efficacy.[7] Among all metal oxides, NiO, owing to its low cost, abundance, chemical stability, and minimum electrical resistance in alkaline medium, is appraised as an excellent material for the electrolytic process. Moreover, CuO is also a nonprecious metal with a large surface area with variable oxidation states, which catalyzes the multielectron transfer reaction, manifesting its strong role in electrocatalysis. When combined, these metal oxides expressed a strong synergistic effect, which imparts extraordinary susceptibility for surface absorption of intermediates and electrical stability, further promoting

[a] *A. Tabassum, S. Ata*
School of Chemistry, University of the Punjab, Lahore, Pakistan
E-mail: sadia.chem@pu.edu.pk

[b] *Y. Ding*
School of Chemical Engineering, University of Birmingham, Birmingham, UK

[c] *I. U. Mohsin*
Institute of Applied Materials-Applied Materials Physics (IAM-AWP), Karlsruhe Institute of Technology, Karlsruhe, Germany

[d] *S. A. K. Leghari*
Pakistan Institute of Engineering and Applied Sciences, Islamabad, Pakistan

[e] *A. A. Al-Kahtani, A. Nafady*
Chemistry Department, College of Science, King Saud University, Riyadh 11451, Saudi Arabia

[f] *M. Sohail*
Department of Chemistry, School of Natural Sciences, National University of Sciences and Technology, Islamabad 44000, Pakistan
E-mail: manzar.sohail@sns.nust.edu.pk

their electrocatalytic performance.[4a,8] Hence, the fabrication of binary NiO–CuO composites can be contemplated as a versatile alternative to noble metals for water cleavage in hydrogen production.

Therefore, this work has applied a straightforward hydrothermal technique to fabricate Ni–Cu binary oxides to get material directly grown on the Ni foam substrate. The directly assembled materials have various advantages over traditional catalysts: interconnected structural networks and spaces that reduce transport distance by making adequate contact between electrode and electrolyte for continuous charge flow; large, exposed surface area for rapid conversion; and improved electrical conductivity for electrochemical reaction. Moreover, the particle size and morphology can be modulated by controlling hydrothermal reaction parameters such as time and temperature. This fabrication process generates highly homogeneous ultrafine nanoparticles having a well-defined composition and shape compared to the other synthetic modes.[9] It is well-studied that various nanostructures, such as sheets, spheres, wires, and needles, greatly influence the electrochemical performance of the materials. Therefore, it is important to form materials with controlled morphology by varying reaction conditions so that they can deliver enhanced catalytic performance.[10] Thus, the hydrothermal route is one of the best for fabricating self-assembled electrode materials with perceptible shapes. On the other hand, OER, for its complexity and lagging kinetics on account of four electron/proton transfer reaction steps, requires the development of an efficient electrocatalyst.[11] Consequently, this research involves binary nickel copper oxides directly deposited on the nickel foam using the hydrothermal method. The growth time was varied from 4 to 24 h to bring morphological changes. The material's performance based on its morphology relative to growth time was explored and regarded as an efficient electrocatalyst for OER in the future.

2. Materials and Methods

2.1. Materials and Synthesis of Ni–Cu Oxides

The bimetallic Ni–Cu oxides have been synthesized using a facile hydrothermal route (Figure 1). The nickel nitrate hexahydrate [Ni $(NO_3)_2$ $6H_2O$], copper nitrate trihydrate [Cu $(NO_3)_2$ $3H_2O$], ammonium fluoride (NH_4F), and urea have been deployed as metal sources, as well as activating and reducing agents. In addition, nickel foam, potassium hydroxide, hydrochloric acid, and ethanol were required. These all were purchased from Sigma-Aldrich. The chemicals were entirely of analytical grade and utilized without any purification procedure.

First, the Ni foam substrate was cut into 1×1.5 cm dimensions and cleansed ultrasonically in 3 M HCl, ethanol, and deionized water for 10 min each, then dried in an oven at 50 °C in a vacuum oven. For Ni–Cu fabrication, 2 mmol of nickel and copper salts were mixed with 12 mmol of NH_4F and 15 mmol of urea in 50 mL of deionized water under constant stirring for 30 min. After the materials were dissolved, the prepared solution was poured into a Teflon autoclave. The Ni foam was also immersed into the autoclave, and the whole container was kept in an oven operating at 160 °C for 4 h. After completion of the reaction, the Ni foam was removed, washed with ethanol and deionized water, and dried for 2 h at 80 °C. Finally, the bimetallic oxides were obtained over the Ni foam after the calcination process in a muffle furnace at 350 °C for 2 h. The structural variations were introduced by repeating the same experimental process for 4, 6, 18, and 24 h. The samples were named NiCu 4, NiCu 6, NiCu 18, and NiCu 24 according to their growth time. Additionally, the catalyst mass loading was computed as 14, 20, 20, and 19 mg, respectively, by weighing nickel foam before and after the hydrothermal reaction.

2.2. Characterization

The crystalline nature of the samples was studied using the X-ray diffraction technique (Model Equinox 3000 Make Thermo Fisher Scientific) targeted with Cu radiation ($\lambda = 0.154$ nm) in the range of 0 to 120°. The functional group's analysis was performed by employing Fourier transform infrared (IR-prestige-21, Shimadzu) and Raman spectroscopy (Xplora Plus Horiba Spectrometer with excitation wavelength of 633 nm) within a wavenumber range of 400–4000 cm^{-1}. The surface morphology was explored by applying field emission scanning electron microscopy (FESEM, Model MAIA 3 TESCAN). All the electrochemical measurements were carried out with the help of an electrochemical workstation/potentiostat (Potentiostat/Galvanostat/ZRA Interface 1000-E Gamry Instrument, USA).

2.3. Electrochemical Characterization and OER Measurements

The electrochemical measurements were conducted using a conventional three-electrode setup, with a Cu–Ni bimetallic sample on Ni foam as a working, Hg/HgO as a counter, and graphite rod as a reference electrode, respectively. The obtained potentials were converted to reversible hydrogen electrode potential without applying iR corrections. All the experiments were managed at room temperature (25 °C) in 1 M potassium hydroxide solution as electrolyte. The OER activities were analyzed by linear sweep polarization curves (LSV) within 0–1.5 V at a 5 mV/sec scan rate. The electrochemical impedance spectroscopy (EIS) was performed within the frequency range of 10 –100 kHz at 10 mV potential. The cyclic voltammetry (CV) was carried out in non-Faradaic regions (0.1–0.23 V) at different scan rates of 20, 40, 60, 80, and 100 mV/sec. The stability check was executed by running 1000 CV cycles at the faster scan rate (200 mV/sec) at a potential of 0–1.0 V. All the activity parameters were computed using standard equations (Supporting Information).

3. Results and Discussion

The XRD patterns for Ni–Cu bimetallic oxides synthesized by varying growth times have been shown in Figure 2a. The pat-

Figure 1. Schematic diagram for fabrication of Ni–Cu bimetallic oxides with various growth time.

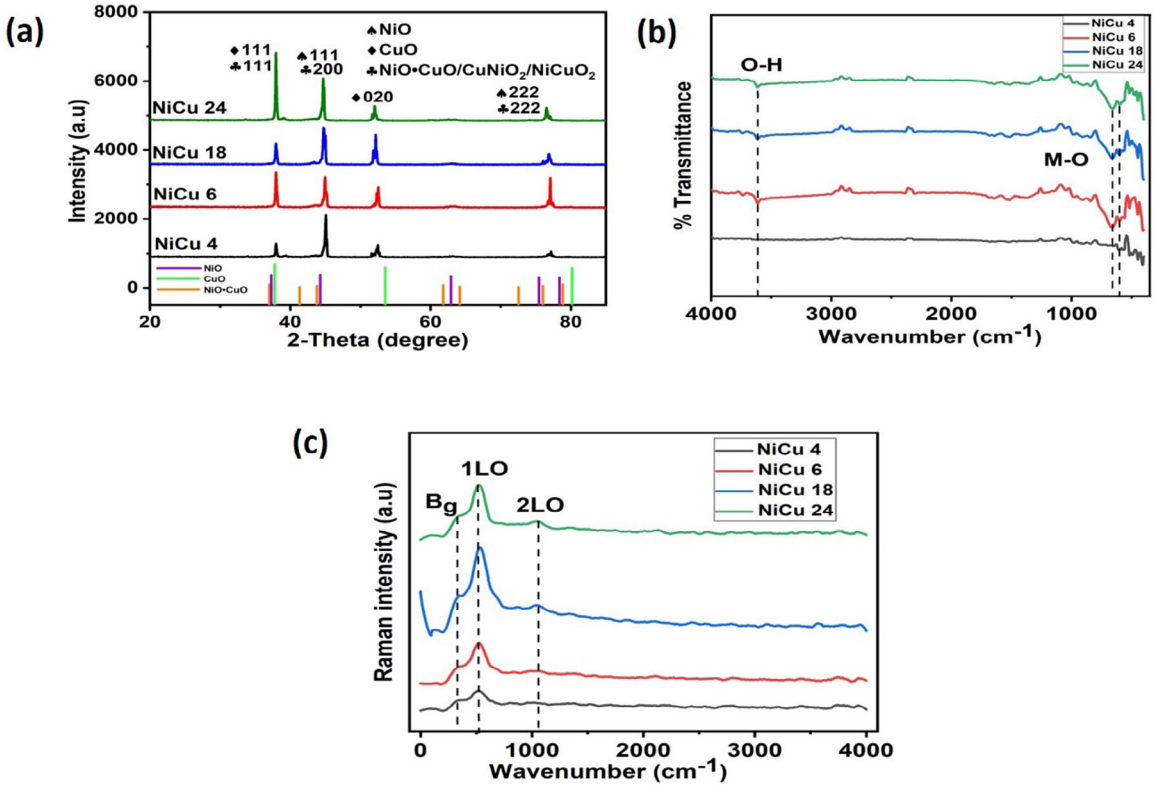

Figure 2. Ni–Cu bimetallic oxides (a) XRD spectra, (b) FTIR spectra, and (c) Raman spectra.

terns revealed sharp, well-defined peaks for all the samples, ensuring their crystalline nature. The peaks that appeared at 2θ degree, indexed to corresponding planes, are as: 37.76 (111) and 53.53 (020) for CuO, 44.29 (111) and 78.84 (222) for NiO, and 37.01 (111), 43.80 (200), and 78.84 (222) for $CuO.NiO/CuNiO_2/NiCuO_2$, respectively. These peaks are well-matched with CuO JCPDS card no. 01-080-1268 (monoclinic), NiO JCPDS card no. 04-0835 (monoclinic), and JCPDS card no. 06-0720 (tetragonal) of Ni–Cu oxide. The spectra also revealed that by increasing the reaction time, the intensity of the peaks also increases, confirming their high crystallinity. No other peak for any impurity has been found to validate the formation of pure NiO and CuO phases. The average crystallite size is estimated as 20, 22, 22.9, and 25 nm for NiCu 4, NiCu 6, NiCu 18, and NiCu 24, respectively, which has been calculated using the Debye–Scherrer Equation (1):

$$D = \frac{K\lambda}{\beta\cos\theta} \tag{1}$$

where D represents crystallite size (nm), K is constant equal to 0.9, λ is the wavelength of incident X-rays (0.1546 nm), β is full width at half maximum of intense peaks, and θ is a diffraction

Table 1. Parameters calculated from XRD data.

Sample	Crystallite Size (nm)	Degree of Crystallinity (%)	Dislocation Density (nm^{-2})
NiCu 4	20	80.01	0.0025
NiCu 6	22	80.20	0.0020
NiCu 18	22.9	80.35	0.0019
NiCu 24	25	81.57	0.0016

angle.[12] The average size of crystallites increases with increasing the reaction time as prolonged contact helps in particle coalescence and thus controls their growth (Ostwald's ripening mechanism). This increasing size has a direct relation with the crystallinity of the particles, as mentioned above.[13] The degree of crystallinity has been calculated by using Equation (2):

$$\text{Degree of crystallilinty} = \frac{\text{Area of crystalline peaks}}{\text{Area of all peaks } (\text{crsytalline} + \text{amorphous})} \times 100 \quad (2)$$

The degree of crystallinity for NiCu 4, NiCu 6, NiCu 18, and NiCu 24 is found to be 80.01, 80.20, 80.35, and 81.57%, respectively. The degree of crystallinity, size, and crystalline phase of the particles strongly affect their properties and reactivity. In some cases, high crystallinity is favorable for the electrocatalytic activity of the catalysts.[14] The high crystalline nature of the particles manifests higher structural stability of the particles and hence results in stable OER performance.[15]

Further, dislocation density (δ) can also be estimated from the crystallite size. The dislocation density represented irregularity/dislocations/defects within a crystal. It can be calculated by using given Equation (3):

$$\delta = \frac{1}{D^2} \quad (3)$$

The dislocation density is inverse to crystallite size, as depicted by the results (Table 1). It can be seen that with an increase in crystallinity, the values for dislocation density have been reduced, which in return confirms the well-arranged crystalline nature of the prepared Ni–Cu oxides.[16] The above parameters calculated from XRD patterns are also shown in Table 1.

The FTIR analysis provides evidence about the oxide's conformation of nanoparticles.[17] Herein, the FTIR spectra (Figure 2b) exhibited almost the same peaks for all the samples of Ni–Cu bimetallic oxides. However, the sample prepared with a growth time of 4 h exhibited a very narrow band within the range of 500–600 cm^{-1}, which may be due to the nonformation (little growth) of metal oxides at this stage. The peak at 3614 cm^{-1} is mainly caused by O—H stretching vibrations of water molecules adsorbed at the surface of the bimetallic catalysts. A sharp peak around 601 cm^{-1} is characteristic of Cu—O linkage, indicating CuO formation.[18] Further, an intense peak at 663 cm^{-1} validated the Ni—O stretching vibrations.[19] Thus, the FTIR results demonstrated the formation of Ni–Cu oxides devoid of impurity.

Raman spectroscopy is an indispensable technique to investigate the structure of nanosized particles based on their atomic arrangements and vibrations.[20] In Figure 2c, Raman spectra displayed three peaks for Ni–Cu bimetallic oxides at 329, 513, and 1040 cm^{-1}, respectively. The Raman spectrum of CuO usually evinced three active modes as 1Ag and 2Bg. Here, the peak at 329 cm^{-1} is well-correlated with the Bg mode of Cu—O stretching vibration, thereby affirming the presence of CuO phase in the prepared samples.[21] Furthermore, the NiO mostly manifested four Raman active modes as 1LO, 2TO, 2TO+2LO, and 2LO. Here, the broad peak at 513 cm^{-1} is assigned to 1LO phonon mode (first-order longitudinal mode of vibration), and the small peak at 1040 cm^{-1} represents 2LO phonon mode (second-order longitudinal mode of vibration) of Ni—O stretching movement.[22] NiO and CuO peaks strongly substantiate the formation of metal oxides in our samples.

The surface structure of the Ni–Cu binary oxides prepared at various growth times under hydrothermal conditions has been depicted by SEM micrographs recorded at different magnifications (Figure 3 and S1). The SEM images clearly exhibit that the particles are grown uniformly over nickel foam, and their shapes are totally dependent on the reaction condition. In this context, the effect of reaction time on the morphology of nanoparticles was investigated. As the reaction time is increased, the particle's sheet-like morphology changes to a very fine thread-like shape. At a reaction time of 4 h, the nanosheets are elongated, uniformly stacked, and cross-linked with each other without any agglomeration. The spaces between the particles are negligible, and the average particle size is found to be 42 nm (the size in nm is calculated using ImageJ software) (Figure 3a–c). The surface morphology was varied further by increasing reaction time by up to 6 h. The particles displayed granular sheet-type morphology. The sheets are smaller and well-interlinked, with an average particle size of 24 nm (Figure 3d–f). At a reaction time of 18 h, the sheet edges become sharp and triangular (Figure 3g–i). The average thickness of the sheets was calculated to be 23 nm. However, with a time of 24 h, the nanosheets were totally modified to a thread-like structure with an even smaller size of 22 nm (Figure 3j–l). The smaller nanoparticle size is considered more beneficial in terms of interaction between the electrode surface and electrolyte, thereby drastically enhancing the electrochemical performance of the materials.[12b] The elemental composition of the samples was determined by EDX analysis (Figure S2). The EDX study demonstrated the presence of Ni, Cu, and O peaks in the spectra. However, the atomic percentages of the elements differ in all the samples according to the reaction time. These results suggested the successful formation of Ni–Cu oxides. Additionally, no other elemental peaks were observed in EDX spectra, certifying the purity of the prepared samples. These results are in accordance with the literature.[23]

4. Electrochemical OER Study

The electrochemical OER performance of Ni–Cu bimetallic oxides fabricated on Ni foam was investigated in 1 M KOH solution as an electrolyte by utilizing a three-electrode system. The LSV are depicted in Figure 4a and Table 2. The main parameter that describes the activeness of the materials for OER is an over-

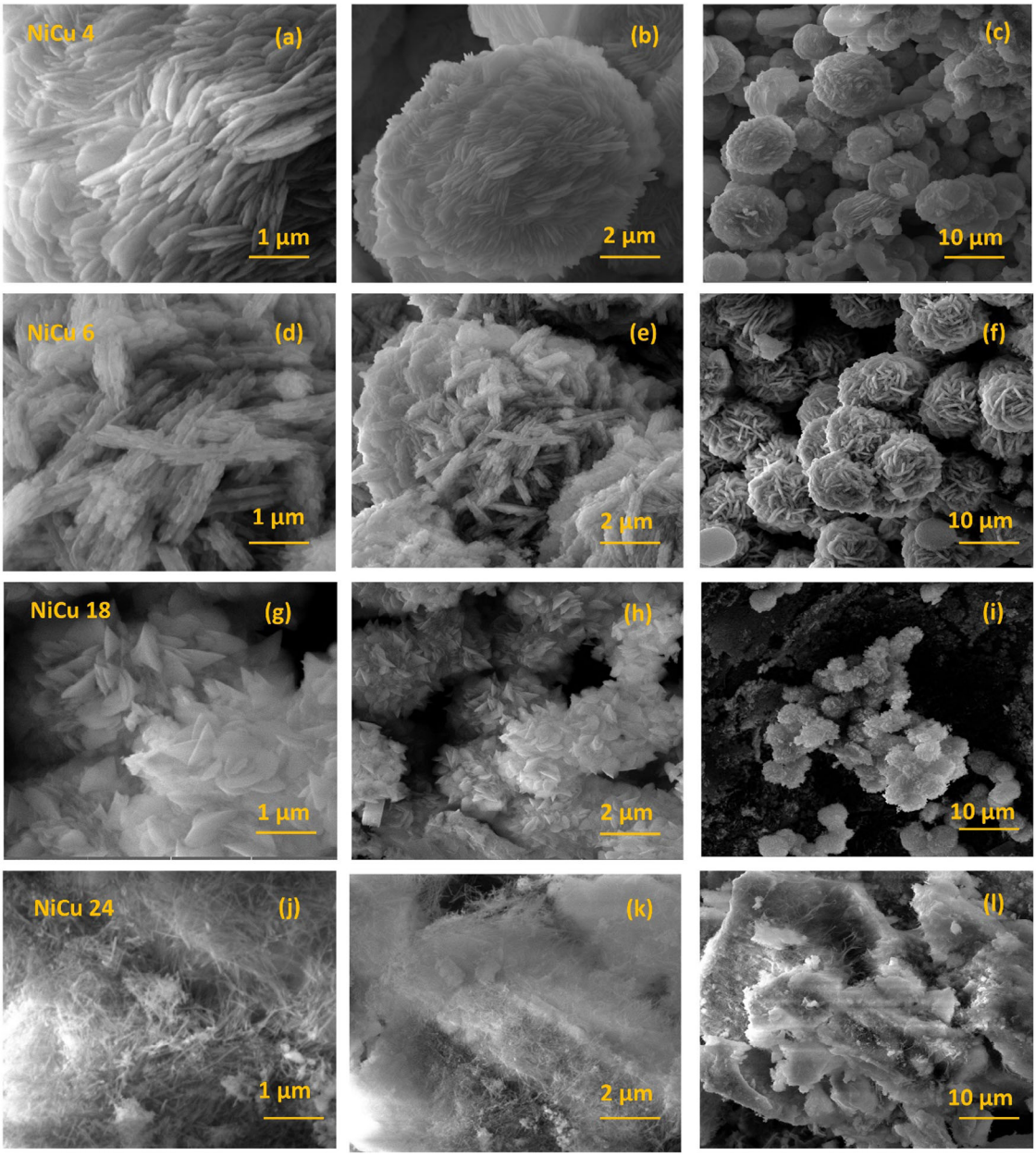

Figure 3. SEM micrographs of Ni–Cu bimetallic oxides at various resolutions of 1 µm, 2 µm, and 10 µm, respectively. (a, b, c) NiCu 4, (d, e, f) NiCu 6, (g, h, i) NiCu 18, and (j, k, l) NiCu 24.

Table 2. Comparison of OER activity data of prepared samples.

Samples	Onset Potential (mV)	Overpotential @10 mA/cm^2 (mV)	R_{ct} (ohm cm^2)	ECSA (cm^2)
NiCu 4	306	438	481	0.02
NiCu 6	310	474	7.929	0.09
NiCu 18	302	507	17.99	0.22
NiCu 24	222	390	2.788	0.24

potential (η) value in mV. The overpotential is narrated as a difference of potential between the ideal thermodynamic potential of 1.23 V versus RHE and the potential need for oxygen evolution at a certain current density (mA/cm^2). The catalyst that exhibits low overpotential values at the same current density will be declared as a highly active material for OER.[24] Herein, the Ni–Cu bimetal oxides prepared at a growth time of 24 h depicted a low onset potential of 222 mV for OER; in addition, this catalyst needed an overpotential of 390 mV to achieve a current density of 10 mA/cm^2. The Ni–Cu oxides with growth times of 4, 6, and 18 h mainly exhibit OER onset potentials of 306, 310, and 302 mV, along with the potentials required to attain a current density of 10 mA/cm^2 are as 438, 474, and 507 mV, respectively. These results are highly comparable with the literature (Table S1).[25] According to the literature, any material that exhibits overpotential in the range of 300–400 mV is considered good for OER performance.[26] It has also

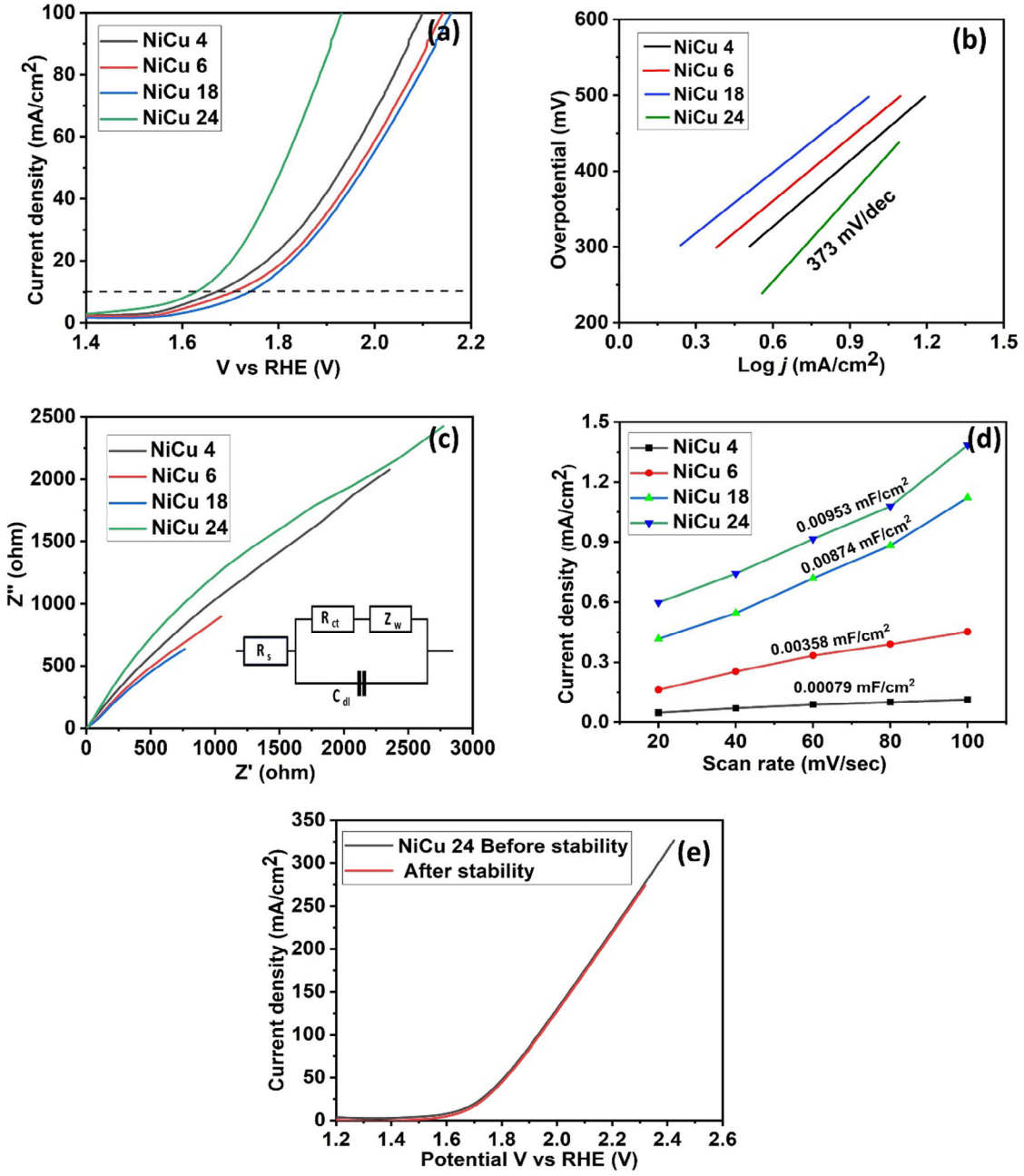

Figure 4. OER performance parameters for Ni–Cu binary oxides (a) LSV polarization curves at 0 ± 1.5 V, (b) Tafel slope, (c) EIS Nyquist plot obtained at 10–100 kHz with Electrical equivalent circuit (EEC) (inset), (d) double-layer capacitance (Cdl), and (e) LSV polarization curve before and after 1000 CV cycles.

been observed that the current density shifted towards a higher range by increasing growth time from 4 to 24 h, as demonstrated by NiCu 24 catalyst in LSV curves. In actuality, the growth time has shown a great impact on the activity of the catalysts, which is observed by the variable surface structure of the Ni–Cu nanoparticles as the shape of the nanoparticles was changed from sheets to threads-like structure. At 24 h of reaction time, the size and spaces among the nanoparticles are very small. These particles are uniformly grown in all directions and ensure a large surface area suitable for better interactions between electrode and electrolyte, thus resulting in enhanced electrochemical activity.[12b]

The Tafel slope, obtained by fitting linear parts of the LSV curve after applying the Tafel equation, is another parameter to estimate the kinetics of the charge transfer process, as a smaller Tafel slope refers to a faster OER rate.[27] The NiCu 24 catalysts exhibit a Tafel slope of 373 mV/dec, whereas NiCu 4, NiCu 6, and NiCu 18 exhibit Tafel slopes of 289, 278, and 267 mV/dec, respectively (Figure 4b). The higher Tafel slope value can be justified by the fact that, during OER, metal oxidation was also taking place at the same time; thus, their combined effect results in the enhanced current density values that affect Tafel slope (as at higher current density, the value of Tafel slope escalates).[28] To further investigate the electronic transfer at

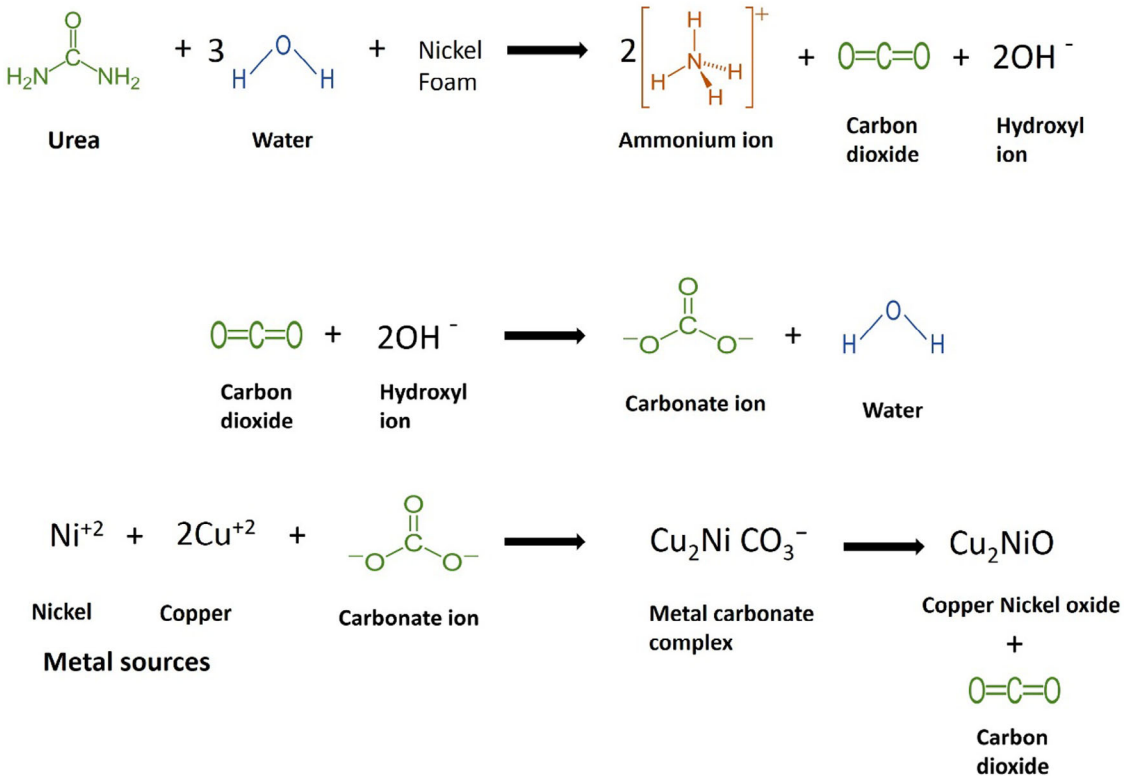

Figure 5. Proposed mechanism for formation of bimetallic Ni–Cu oxides.[39]

the electrode/electrolyte interface, EIS was applied from 10 to 100 kHz.[29] Nyquist plots and electrical equivalent circuits (EEC) are given in Figure 4c. Here, R_s, R_{ct}, $Z_{w,}$ and C_{dl} represented solution resistance, charge transfer resistance, Warburg resistance, and double-layer capacitance, respectively.[30] The charge transfer resistance (R_{ct}) was computed by fitting an electrical equivalent circuit to the Nyquist plots as 481.4, 7.929, 17.94, and 2.788 ohm cm^2 for NiCu 4, NiCu 6, NiCu 18, and NiCu 24, respectively. The lower R_{ct} value usually depicts a faster transfer of electrons, just as the catalysts NiCu 24 indicated here, confirming its faster kinetics, leading to better OER performance. Another significant parameter for determining the charge transfer rate is exchange current density (I_{ex}) calculated as 0.013, 0.809, 0.357, and 2.302 mA/cm^2 for NiCu 4, NiCu 6, NiCu 18, and NiCu 24, respectively. Notably, NiCu 24 has a large exchange current density value as compared to other catalysts; thus, proposing faster transfer of charges at the electrode and electrolyte interface, leading to its high efficacy towards OER.[31] Furthermore, to gain insights into the OER mechanism, the double-layer capacitance (C_{dl}) was assessed from slope values of the plot between current densities at various scan rates for all the samples (Figure 4d). The double-layer capacitance is greatly dependent on the electrochemically active surface area of the catalyst material. A higher value of double-layer capacitance indicates better access to the active sites on the electrode surface.[32] It is evident from the results that NiCu 24 displayed a larger value of C_{dl}, 0.00953 mF, relative to other catalysts. The NiCu 4, NiCu 6, and NiCu 18 have C_{dl} values of 0.00079, 0.00358, and 0.00875 mF, respectively. The electrochemical surface area (ECSA) was calculated from the C_{dl} values as they are in the linear relationship.[33] The NiCu 24 exhibited a large surface area of 0.24 cm^2, whereas NiCu 4, NiCu 6, and NiCu 18 manifested a surface area of 0.02, 0.09, and 0.22 cm^2, respectively.

Catalyst's durability is also crucial for practical implementations. The stability check of NiCu 24 was performed for 1000 CV cycles at faster scan rates within the potential of 1.0 V (Figure 4e, S4). The catalyst represented strong stability in this range without any changes and is considered an effective material for OER performance. Nanostructuring linked with morphological changes is a straightforward pathway for enhancing catalytic activity by providing more active sites within a specific surface area. The OER activity for NiCu 24 could be explained by increasing growth time; the nanoparticles gain ultrasmall size with thread-like structure (very fine nanosheets). The uniformly distributed nanoparticles allow faster charge transfer through their void spaces, escalating OER catalysis. These results strongly suggested that morphological changes greatly impact the activity of any catalysts, and thus play a pivotal part in developing effective materials for future use.[34] It is also assumed that the long hydrothermal reaction time converts initially disordered nanosheets to highly ordered or well-defined crystalline and stable nanosheets, which are considered more OER active. Furthermore, as discussed earlier, the reaction parameters are also decisive in adjusting the morphology of the samples. It is inferred that urea plays a significant role in the formation of nanosheets. During the hydrothermal reaction, the urea was thermally decomposed to ammonia (precipitating agent) and carbon dioxide, which are involved in maintaining the pH of

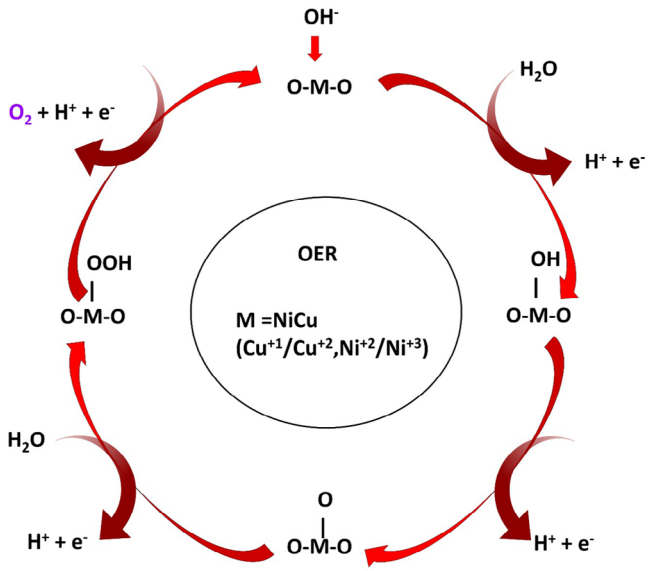

Figure 6. OER mechanism on the surface of Ni–Cu bimetallic oxides.

the solution (the proposed mechanism for Ni–Cu bimetallic oxides formation is depicted in Figure 5). Such urea hydrolysis is a widely accepted technique for producing layered-type nanostructures.[35] The mechanism of OER on the surface of catalysts under an alkaline medium is four-electron transfer steps. It can also be explained well based on the synergistic effect of both metals (Figure 6). The higher oxidation states of the metals Cu^{+2} and Ni^{+3} are crucial for excellent water oxidation reactions.[36] These findings strongly reflected better OER results regarding overpotential values and agree with the existing literature.[37] The OER performance is evaluated in a strongly alkaline medium under high potential, which can induce structural or chemical changes in the electrocatalyst. Therefore, a postcatalysis analysis was conducted after the stability check using XRD measurements. No significant or noticeable changes have been observed except for little enhancement in peaks of NiO, which may arise due to Ni foam used as a support. This suggested NiCu 24 stability in an alkaline KOH solution (Figure S5).[38]

5. Conclusion

In this work, we have reported hydrothermally synthesized Ni–Cu bimetal oxides directly fabricated over nickel foam by varying growth time to induce morphological changes coupled with nanosizing. The growth time was extended from 4 to 24 h. The results demonstrated visible shape fluctuations with increasing reaction time. The Ni–Cu prepared at a reaction time of 24 h displayed better OER activity with a low onset potential of 222 mV and a Tafel slope of 373 mV/dec. The catalyst also exhibited a larger ECSA of 0.24 cm^2, declaring its superior activity in abundant active sites. The results clearly emphasized that nanosheet-like morphological variations of Ni–Cu bimetallic oxides have huge potential for OER and offer advantages over noble metals, being environmentally benign for future usage.

Acknowledgements

The authors extend their sincere appreciation to the Researchers Supporting Project number (RSP2024R266) at King Saud University, Riyadh, Saudi Arabia, for partial support of this work.

Conflict of Interests

The authors declare no conflict of interest.

Data Availability Statement

The data that support the findings of this study are available from the corresponding author upon reasonable request.

Keywords: Electrochemical water oxidation · Hydrothermal method · Nanosheets · Ni–Cu bimetallic oxides · Self-standing

[1] a) M. Tang, Y. Liu, H. Cao, Q. Zheng, X. Wei, K. H. Lam, D. Lin, *Int. J. Hydrogen Energy* **2022**, *47*, 3013–3021; b) D. Chinnadurai, R. Rajendiran, P. Kandasamy, *J. Colloid Interface Sci.* **2022**, *606*, 101–112.

[2] a) X. Zou, Y. Zhang, *Chem. Soc. Rev.* **2015**, *44*, 5148–5180; b) H. K. Zafar, S. S. A. Shah, M. Sohail, R. S. Ashraf, A. Nafady, G. Will, M. A. Wahab, *J. Power Sources* **2024**, *612*, 234827.

[3] S. Li, M. Li, Y. Ni, *Appl. Catal. B Environ.* **2020**, *268*, 118392.

[4] a) J. Niu, Y. Yue, C. Yang, Y. Wang, J. Qin, X. Zhang, Z.-S. Wu, *Appl. Surf. Sci.* **2021**, *561*, 150030; b) A. Hassan, H. K. Zafar, R. Shahid Ashraf, M. Arfan, M. Rezaul Karim, M. A. Wahab, M. Sohail, *Chem. Asian J.* **2024**, *19*, 1–10.

[5] R. Gao, M. Deng, Q. Yan, Z. Fang, L. Li, H. Shen, Z. Chen, *Small Methods* **2021**, *5*, 2100834.

[6] L. Zhang, H. Gong, *Electrochim. Acta* **2017**, *234*, 82–92.

[7] a) A. J. Laghari, U. Aftab, A. Tahira, M. Y. Solangi, A. A. Hulio, G. M. Thebo, M. I. Abro, M. A. Bhatti, S. Kumar, E. Dawi, A. Nafady, A. Infantes-Molina, M. Emo, B. Vigolo, Z. H. Ibupoto, *J. Cluster Sci.* **2024**, *35*, 1941–1958; b) N. Tahir, A. Altaf, N. Baig, A. Nafady, A. Ul-Hamid, S. S. A. Shah, P. Tsiakaras, M. Sohail, *Chem. Asian J.* **2024**, *19*, e202301100; c) W. Adamson, X. Bo, Y. Li, B. H. Suryanto, X. Chen, C. Zhao, *Catal. Today* **2020**, *351*, 44–49.

[8] N. Sandhiran, S. Ganapathy, Y. Manoharan, D. Ganguly, M. Kumar, K. Ramanujam, S. Balachandran, *Environ. Res.* **2022**, *211*, 112992.

[9] S. Rendale, S. Beknalkar, A. Teli, J. Shin, T. Bhat, *J. Electroanal. Chem.* **2023**, *932*, 117253.

[10] W. Sun, X. Ling, W. Wei, H. Hu, Z. Jiang, Z. Yan, J. Xie, *Appl. Surf. Sci.* **2019**, *493*, 710–718.

[11] S. Song, J. Zhou, J. Sun, S. Zhang, X. Lin, Z. Hu, J. Hu, L. Zhang, J.-Q. Wang, *Chin. J. Catal.* **2020**, *41*, 592–597.

[12] a) A. Iqbal, A. u. Haq, G. A. Cerrón-Calle, S. A. R. Naqvi, P. Westerhoff, S. Garcia-Segura, *Catalysts* **2021**, *11*, 806; b) M. Yewale, R. Kadam, N. Kaushik, N. Linh, A. Teli, J. Shin, L. Lingamdinne, J. Koduru, D. Shin, *Chem. Phys. Lett.* **2022**, *800*, 139654; c) C.-S. Song, C. V. M. Gopi, R. Vinodh, S. Sambasivam, R. M. N. Kalla, I. M. Obaidat, H.-J. Kim, *J. Energy Storage* **2019**, *26*, 101037.

[13] a) G. Collazzo, S. Jahn, N. Carreño, E. Foletto, *Braz. J. Chem. Eng.* **2011**, *28*, 265–272; b) A. M. Teli, S. A. Beknalkar, S. M. Mane, L. S. Chaudhary, D. S. Patil, S. A. Pawar, H. Efstathiadis, J. C. Shin, *Appl. Surf. Sci.* **2022**, *571*, 151336.

[14] Y. Li, L. A. Zhang, Y. Qin, F. Chu, Y. Kong, Y. Tao, Y. Li, Y. Bu, D. Ding, M. Liu, *ACS Catal.* **2018**, *8*, 5714–5720.

[15] J. Xu, X. Zhu, X. Jia, *ACS Sustainable Chem. Eng.* **2019**, *7*, 16629–16639.

[16] a) R. Jacob, H. G. Nair, J. Isac, *Int. Lett. Chem. Phys. Astron.* **2015**, *41*, 100–117; b) A. F. Abdulrahman, A. A. Barzinjy, S. M. Hamad, M. A. Almessiere, *ACS Omega* **2021**, *6*, 31605–31614.

[17] Z. N. Kayani, M. Umer, S. Riaz, S. Naseem, *J. Electron. Mater.* **2015**, *44*, 3704–3709.

[18] A. A. Radhakrishnan, B. B. Beena, *Indian J. Adv. Chem. Sci.* **2014**, *2*, 158–161.

[19] S. D. Khairnar, V. S. Shrivastava, *J. Taibah Uni. Sci.* **2019**, *13*, 1108–1118.

[20] K. R. Reddy, *J. Mol. Struct.* **2017**, *1150*, 553–557.

[21] J. Xu, W. Ji, Z. Shen, S. Tang, X. Ye, D. Jia, X. Xin, *J. Solid State Chem.* **1999**, *147*, 516–519.

[22] S. Amin, A. Tahira, A. Solangi, R. Mazzaro, Z. H. Ibupoto, A. Vomiero, *Anal. Methods* **2019**, *11*, 3578–3583.

[23] G. Gnanamoorthy, V. Karthikeyan, D. Ali, G. Kumar, V. K. Yadav, V. Narayanan, *Environ. Res.* **2022**, *204*, 112338.

[24] K. Maslana, K. Wenelska, M. Biegun, E. Mijowska, *Appl. Catal. B Environ.* **2020**, *266*, 118575.

[25] a) C. R. Dhas, S. E. S. Monica, K. Jothivenkatachalam, A. J. Nathanael, V. Kavinkumar, R. Venkatesh, D. Arivukarasan, *Ionics* **2021**, *28*, 383–396; b) A. Roy, H. S. Jadhav, M. Cho, J. G. Seo, *J. Ind. Eng. Chem.* **2019**, *76*, 515–523; c) D. Cao, D. Cheng, *Chem. Commun.* **2019**, *55*, 8154–8157; d) C. Li, B. Zhang, Y. Li, S. Hao, X. Cao, G. Yang, J. Wu, Y. Huang, *Appl. Catal. B Environ.* **2019**, *244*, 56–62.

[26] M. Tahir, L. Pan, F. Idrees, X. Zhang, L. Wang, J.-J. Zou, Z. L. Wang, *Nano Energy* **2017**, *37*, 136–157.

[27] J. Ma, A. Cai, X. Guan, K. Li, W. Peng, X. Fan, G. Zhang, F. Zhang, Y. Li, *Int. J. Hydrogen Energy* **2020**, *45*, 9583–9591.

[28] M. E. Lyons, R. L. Doyle, M. P. Brandon, *Phys. Chem. Chem. Phys.* **2011**, *13*, 21530–21551.

[29] I. Madakannu, I. Patil, B. A. Kakade, K. R. D. Kasibhatta, *Mater. Chem. Phys.* **2020**, *252*, 123238.

[30] Z. U. Rehman, M. A. Raza, U. N. Chishti, A. Hussnain, M. F. Maqsood, M. Z. Iqbal, M. J. Iqbal, U. Latif, *Arabian J. Sci. Eng.* **2022**, *48*, 8371–8386.

[31] F. Arshad, T. ul Haq, A. Khan, Y. Haik, I. Hussain, F. Sher, *Energy Convers. Manage.* **2022**, *254*, 115262.

[32] K. Wan, J. Luo, X. Zhang, P. Subramanian, J. Fransaer, *Int. J. Hydrogen Energy* **2020**, *45*, 8490–8496.

[33] S. Si, H.-S. Hu, R.-J. Liu, Z.-X. Xu, C.-B. Wang, Y.-Y. Feng, *Int. J. Hydrogen Energy* **2020**, *45*, 9368–9379.

[34] B. Paul, P. Bhanja, S. Sharma, Y. Yamauchi, Z. A. Alothman, Z.-L. Wang, R. Bal, A. Bhaumik, *J. Colloid Interface Sci.* **2021**, *582*, 322–332.

[35] P. Madhusudan, J. Ran, J. Zhang, J. Yu, G. Liu, *Appl. Catal. B: Environ.* **2011**, *110*, 286–295.

[36] A. Kumar, S. K. Purkayastha, A. K. Guha, M. R. Das, S. Deka, *ACS Catal.* **2023**, *13*, 10615–10626.

[37] a) S. Rana, K. K. Yadav, S. K. Guchhait, S. T. Nishanthi, S. K. Mehta, M. Jha, *J. Mater. Sci.* **2021**, *56*, 8383–8395; b) B. Chen, P. Hu, F. Yang, X. Hua, F. F. Yang, F. Zhu, R. Sun, K. Hao, K. Wang, Z. Yin, *Small* **2023**, *19*, 2207177; c) S. Natarajan, V. Duraisamy, M. Subramani, S. M. S. Kumar, S. Ponnusamy, *Catal. Commun.* **2023**, *184*, 106796.

[38] C. Andronescu, S. Barwe, E. Ventosa, J. Masa, E. Vasile, B. Konkena, S. Möller, W. Schuhmann, *Angew. Chem. Int. Ed.* **2017**, *56*, 11258–11262.

[39] Y. Jin, L. Wang, Q. Jiang, X. Du, C. Ji, X. He, *Mater. Lett.* **2016**, *168*, 166–170.